Direct observation of turbulent magnetic fields in hot, dense laser produced plasmas

Sudipta Mondal[a], V. Narayanan[a], Wen Jun Ding[b], Amit D. Lad[a], Biao Hao[b], Saima Ahmad[a], Wei Min Wang[b], Zheng Ming Sheng[b,c,1], Sudip Sengupta[d], Predhiman Kaw[d], Amita Das[d,1], and G. Ravindra Kumar[a,1]

[a]Tata Institute of Fundamental Research, 1- Homi Bhabha Road, Mumbai 400005, India; [b]Beijing National Laboratory of Condensed Matter Physics, Institute of Physics, Chinese Academy of Sciences, Beijing 100190, China; [c]Laboratory for Laser Plasmas (Ministry of Education) and Department of Physics, Shanghai Jiao Tong University, Shanghai 200240, China; and [d]Institute for Plasma Research, Bhat, Gandhinagar 382428, India

Edited by* Margaret M. Murnane, University of Colorado at Boulder, Boulder, CO, and approved April 9, 2012 (received for review January 24, 2012)

Turbulence in fluids is a ubiquitous, fascinating, and complex natural phenomenon that is not yet fully understood. Unraveling turbulence in high density, high temperature plasmas is an even bigger challenge because of the importance of electromagnetic forces and the typically violent environments. Fascinating and novel behavior of hot dense matter has so far been only indirectly inferred because of the enormous difficulties of making observations on such matter. Here, we present direct evidence of turbulence in giant magnetic fields created in an overdense, hot plasma by relativistic intensity ($10^{18}\mathrm{W/cm^2}$) femtosecond laser pulses. We have obtained magneto-optic polarigrams at femtosecond time intervals, simultaneously with micrometer spatial resolution. The spatial profiles of the magnetic field show randomness and their *k* spectra exhibit a power law along with certain well defined peaks at scales shorter than skin depth. Detailed two-dimensional particle-in-cell simulations delineate the underlying interaction between forward currents of relativistic energy "hot" electrons created by the laser pulse and "cold" return currents of thermal electrons induced in the target. Our results are not only fundamentally interesting but should also arouse interest on the role of magnetic turbulence induced resistivity in the context of fast ignition of laser fusion, and the possibility of experimentally simulating such structures with respect to the sun and other stellar environments.

intense laser matter interaction | high energy density | astrophysical simulations | filamentary structures

The largest terrestrially available magnetic fields are generated when an intense laser pulse (intensity above $10^{18}\mathrm{W/cm^2}$) irradiates a solid target (1–3). The high energy density produced by laser irradiation generates relativistic electron jets, through the process of wave breaking. These relativistic electron jets carry the laser energy deep into the target ionizing and heating the colder portions behind the laser generated plasma and exciting return shielding currents. In the laboratory, such heating is extremely important for fast ignition of highly compressed targets in laser fusion (4, 5), simulation of intra planetary matter existing at ultrahigh pressure (6), ultrafast X-ray pulses (7), as well as proton and ion acceleration up to the MeV-GeV levels (3). It also serves as an excellent tool for modeling astrophysical systems (8–10). The transport of relativistic electrons through hot dense matter is very complex and is barely understood (11, 12). Simulations have shown that relativistic electron transport in plasma media is fraught with severe plasma instabilities particularly the Weibel instability (13), which leads to spatial separation of forward and backward currents and eventually to the emergence of turbulent structures (14) and rapid energy dissipation. A major physical parameter that mirrors this complex physics is the giant magnetic field—as high as hundreds of megagauss—generated in this interaction. In earlier studies (15–17), we have shown that the temporal evolution of this megagauss magnetic field can provide essential and very useful information on the transport process—for instance, the conductivity of the hot, dense matter and the penetration depth of the hot electrons can be estimated easily. These parameters are not easily obtainable by other methods. In the present study, we take a further leap by spatially resolving the giant magnetic field on a micrometer scale at each temporal delay. These spatial maps clearly show the filamentary structures of electron currents in the plasma. A spectral analysis of these maps indicates that the magnetic fields are turbulent in nature (18). We use pump-probe Cotton–Mouton polariscopy (15–17, 19) to measure the temporal and spatial evolution of the giant magnetic field (the former on picosecond time scale and the latter on micrometer scale). These polarigrams capture the temporal evolution of the filamentation process and a Fourier analysis of the spatial images clearly shows a broad spectrum with a power-law behavior for the magnetic energy. Our analytical studies and two-dimensional particle-in-cell (2D-PIC) simulations support the broad power-law spectrum and clearly demonstrate the presence of turbulence (20, 21).

Magnetic Field: Temporal and Spatial Profiles

Our measurements of the giant magnetic field (shown by the schematic of Fig. 1) are based on the modification of the polarization state of a weak probe beam (400 nm wavelength, 80 fs duration) launched into the plasma at a certain time delay from the plasma producing pump beam of intensity $10^{18}\mathrm{W/cm^2}$ (800 nm wavelength, 30 fs duration). The plasma is created on an optically planar solid target. The probe beam is reflected from the electron density surface in the plasma that is critical for the 400 nm radiation. From the ellipticity induced in the polarization of the reflected probe beam (19), we infer the magnetic field by solving the Helmholtz equation in the plasma using an appropriate electron density profile and scale length. We also run 2D-PIC simulations for our experimental parameters to back the results and provide a detailed interpretation of the observations.

Fig. 2*A* shows the measured time resolved and spatially integrated ellipticity and magnetic field. The ellipticity rises to a maximum of 0.53 in 5.3 ps. The magnetic field increases from 0 to 63 megagauss in 3.2 ps at the critical surface of the probe (400 nm) and starts decreasing beyond this time. Magnetic field strength is along expected lines (1, 2, 15–17). Fig. 2 *B* and *C* shows the results of our 2D-PIC simulations, which will be discussed a little later.

Fig. 2*D* shows a typical spatial profile of the magnetic field and Fig. 2*E* is the corresponding two-dimensional contour plot of the transverse profile of the magnetic field captured at 3.2-ps delay. Note that the transverse dimension of the probe pulse (approximately 60 μm) is approximately three and a half times the trans-

---

Author contributions: G.R.K. designed research; S.M., V.N., A.D.L., S.A., and G.R.K. performed research; S.M., V.N., W.J.D., A.D.L., B.H., S.A., W.M.W., Z.M.S., S.S., P.K., A.D., and G.R.K. analyzed data; W.J.D., B.H., W.M.W., and Z.M.S. performed the PIC simulations; A.D. steered the discussion on turbulence; and S.M., A.D.L., Z.M.S., A.D., and G.R.K. wrote the paper.

*This Direct Submission article had a prearranged editor.

[1]To whom correspondence may be addressed. E-mail: grk@tifr.res.in or zmsheng@sjtu.edu.cn or amita@ipr.res.in.

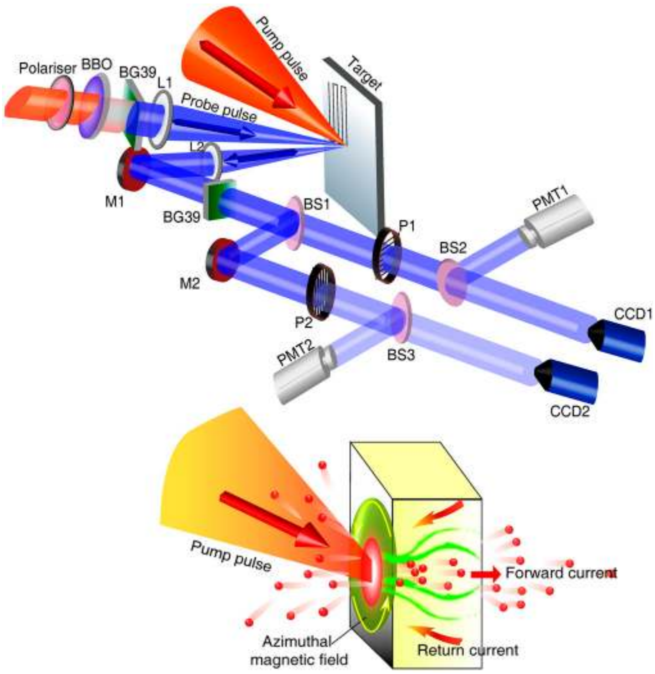

Fig. 1. Sketch of the experimental arrangement for measuring spatial and temporal profiles of the magnetic field. The plasma is created a by an intense pump pulse. A weak probe pulse samples the plasma at different time delays after pump irradiation. The target is an optically polished aluminum coated BK-7 glass plate. BBO, β-barium borate (second harmonic generating crystal); L, Lens; BS, beam splitter; M, mirror; P, polarizer; BG39, Schott glass filter; PMT, photomultiplier tube; CCD, charged couple device camera. The sketch at bottom shows the relativistic hot electron forward currents induced by the pump pulse and the thermal (cold) return currents provided by the target environment. The azimuthal direction of the magnetic field at the critical surface is shown.

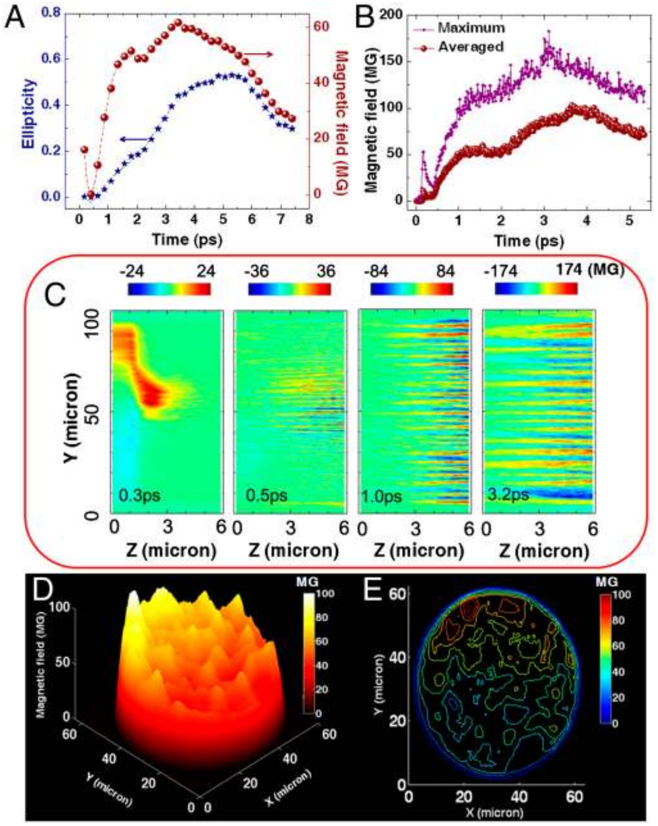

Fig. 2. Magnetic field at the critical surface of the plasma measured with a 400-nm probe pulse. (*A*) Time resolved but spatially integrated ellipticity of reflected probe pulse and the magnetic field derived from this ellipticity. (*B*) Integrated magnetic field derived from 2D-PIC simulation including electron–ion collisions. (*C*) Snapshots of the magnetic field simulation at several time intervals. The filamentation of the currents and localization of the magnetic field is clearly seen. (*D*) Three-dimensional representation, and (*E*) two-dimensional contour plot of space and time resolved magnetic field measured at 3.2 ps.

verse dimension of the pump focal spot and thus is suitable for measuring magnetic fields having transverse structures larger than the pump focal spot. The observed magnetic field is cylindrically asymmetric. We believe that this could be partially attributed to the asymmetric radiation forces on the electrons by the laser pulse (22). The obliquely incident laser pulse pushes the electrons along its propagation direction, inducing this asymmetry, seen in all the images (Fig. 3). This feature is also seen in our 2D-PIC simulations (Fig. 2*C*). The maximization of the magnetic field (over picosecond time scales), long after the incidence of the laser pulse (femtosecond time scale) and its subsequent decay over a period of several picoseconds is similar to that observed in earlier experiments (15–17) and can be understood as follows. The pump laser produces hot energetic electrons at the critical density surface. These electrons propagate inward and the resulting space charge and induction field generate a return shielding current of the background “cold” electrons (14, 23). As has been observed in a variety of PIC simulation studies (24–27), at an initial stage the two currents spatially overlap and the resultant magnetic field is zero. The currents subsequently get Weibel separated, wherein quasi-static ordered magnetic field configurations get generated. This is followed by the tearing and coalescence instabilities, which produce current channels and hence filamentary magnetic field structures. The dynamical formation of these structures occurs on a time scale much shorter than a picosecond and initiates from a spatial scale of order $c/\omega_p \sim 0.1$ μm (where c is the speed of light and ω_p is the plasma frequency), which is much smaller than our spatial resolution (approximately 4 μm). Hence these fine scale spatio-temporal features cannot be captured in our experiments. However, the subsequent turbulence generation [due to mechanism such as fluid like velocity shear driven Kelvin–Helmholtz (KH) like instability arising due to the current shear in spatially separated forward and return shielding currents (12, 28, 29)], leads to the formation of random filamentary magnetic fields, which are sustained over much longer time scales. Our present experimental observation falls in this particular time scale regime for which we provide a detailed analysis.

Filamentary Structures

The magnetic field spatial profiles presented here provide direct pictures of filamentation (Fig. 3). So far filamentation has been seen indirectly in experiments [via spatial profiles of fast electron beams (30), spatial profiles of accelerated proton beams (31), or via optical emission from the target rear (32)]. These provide indirect and somewhat incomplete evidence in the sense that (*i*) they do not directly measure/reflect the current structures inside the target but are inferred from secondary effects, (*ii*) signals are measured outside the target and not in situ, and (*iii*) they are not time resolved. In contrast, we present evolution of the filamentary structures (a) right at the critical surface and (b) resolved all the way upto 7.0 ps—i.e., long after the pump irradiation. Theoretical expectations and simulations (13, 33) suggest that the Weibel separated and tearing destabilized filament thickness should be of the order of c/ω_p (approximately 0.1 μm). The typical thickness of a filament we measure is approximately 4 μm (Fig. 2*E*), indicating that the coalescence of several filaments has occurred. According to simulations the process of Weibel separation and tearing instability for filament formation occurs on the time scale of a few tens of femtoseconds (13) and hence

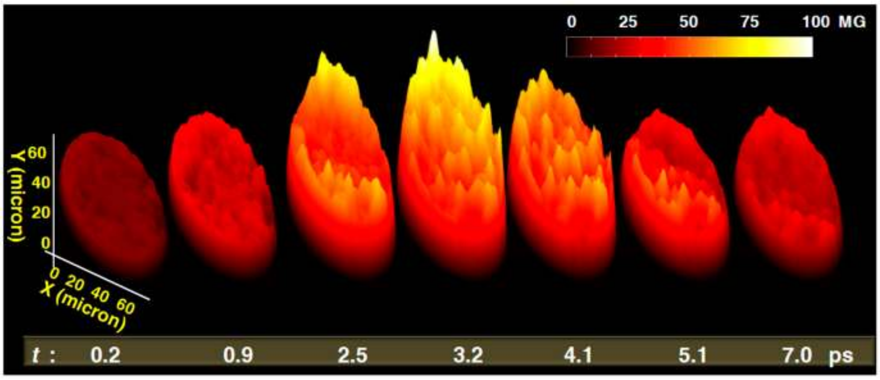

Fig. 3. Complete dynamics of spatio-temporal evolution of the intense laser induced magnetic field at the critical surface of the plasma measured with a 400-nm probe pulse.

can not be captured in present experimental observations. Our studies capture the structures after some coalescence has taken place and monitor the subsequent evolution and long term behavior.

The experimentally measured time evolution of the magnetic field is very well reproduced by the 2D-PIC simulations (Fig. 2*B*), which show that the magnetic field increases with time until around 3.5 ps and then begins to decrease. The lower curve in Fig. 2*B* is obtained by a spatial average along the direction of the plasma density gradient from n_c to $4n_c$. This gives a magnetic field value slightly larger than the experimental value because the latter is a temporal and spatial average. As shown in Fig. 2*C*, the magnetic field structure is determined by the hot electron source produced by the incident laser pulse at the intital stage (0.3 ps). Later, filamentation of the laser produced electron beams and the associated cold return currents develops due to the Weibel-like instability. Localization of the magnetic field is evident at times larger than 0.3 ps. It is found that, collisional resistivity strongly influences the motion of both cold plasma electrons and energetic beam electrons (34), which dominates the long time (multipicosecond) behavior of currents and associated high magnetic fields.

Turbulent Magnetic Field

There is much more information hidden in the measured spatial structures. Fig. 4 presents the power spectrum of images at several time delays. The power spectrum gives the power contained in each spatial mode. To elucidate the measured spatial structure of the magnetic field, we present the 1D power spectrum obtained from the 2D power spectrum by integrating along one spatial dimension (see *Methods* for more details). The spatial structure of magnetic field profile in the transverse plane indeed exhibits considerable randomness right from the data at 0.2 ps to the last observation shown at 7.0 ps. The spatial randomness of the measured magnetic field profiles provides a strong direct indication for turbulence. A broad power-law Fourier spectrum obtained by analyzing dozens of such images (details are described in *Methods*) is yet another pointer toward the turbulent nature of the phenomenon (18, 20, 21). The spatial power spectra have an identical form for all times though the spatial transverse profile of magnetic field appear significantly different at each instant (Fig. 4). The form remains identical albeit the spectral intensities at various scales show a steady increase up to 3.2 ps and a decay beyond this time. Further, the spectrum shows three distinct peaks occurring around three harmonics—namely, k, $2k$, and $3k$ with $k \approx 7$ (in units of inverse electron skin depth) in all the datasets. The spectra fit a power law $k^{-\alpha}$ with an index that is close to $\alpha = 2$. In short, the transverse spatial magnetic field profile shows the following characteristic features: (*i*) random spatial pattern in transverse plane of the target which has a maximum amplitude at =3.2 ps; (*ii*) identical form of the spectra for all times; (*iii*) spectral peaks at the first, second, and third harmonic of k with $k \approx 7$; (*iv*) the spectra fits a power law $\sim k^{-2}$.

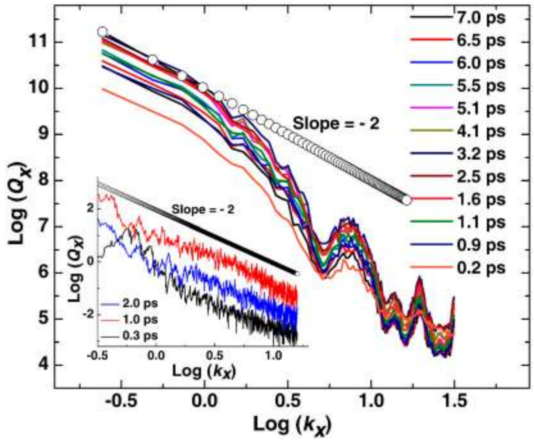

Fig. 4. Power spectrum of magnetic field spatial profiles measured at different pump-probe delays. The inset shows the power spectra derived from 2D-PIC simulations.

The inset of Fig. 4 shows the power spectrum derived from our 2D-PIC simulations. It can be seen from this figure that the spectrum follows a power-law k^{-2} similar to the experimental results, in particular at the later stages of evolution. The results for the magnetic field are not much sensitive to the initial electron temperatures. The final electron temperature is in the range of 300–600 keV and ion temperature in the range 4–8 keV. The cell size in our simulation prevents the retrieval of the sharp features seen in the experiment.

These features can be readily understood on the basis of an electron magnetohydrodynamic (EMHD) description. The forward and return shielding currents get spatially separated as a result of Weibel instability during the initial femtoseconds of evolution (13). The subsequent tearing and coalescence instabilities generate current channels with sheared electron flow configuration. This sheared electron flow configuration is susceptible to KH like instability and may be responsible for turbulence in the magnetic field, resulting in a broad power spectrum. Furthermore, as the separated current pulse moves toward a high density plasma (it has to traverse from the critical density of n_c to $4n_c$, where observations are made) it encounters plasma density inhomogeneity and forms structures sharper than the electron skin depth by the mechanism outlined in our earlier work (27). We believe this may be responsible for the multiple peaks observed in the spectrum at scales much sharper than the electron skin depth.

Let us now estimate the value of the Reynolds like parameter (the typical ratio of nonlinearity to dissipation pertinent to the system) for our experiments. Here this will be provided by $Re_{\mathrm{exp}} = \vec{v}\cdot\nabla\vec{v}/\nu_{\mathrm{ei}}\vec{v}$, the dominant dissipation being the resistivity arising out of the electron-ion classical collision frequency. For fast electrons $v \sim c$ and taking the typical scales of filaments to be of the order of skin depth, we have $Re_{\mathrm{exp}} \sim \omega_{\mathrm{pe}}/\nu_{\mathrm{ei}} \sim 10^6$ a reasonable value for the turbulence to set in (18, 20, 21). We also wish to point out that, the energy spectrum for EMHD turbulence have been predicted to be (35) around $-7/3$ (~ -2.33) for $k \ll 1$, and $-5/3$ (~ -1.66) for $k \gg 1$, which are numbers quite close to -2.

Conclusions

In conclusion, we have presented direct evidence for turbulence in the megagauss magnetic fields generated by relativistic electron currents induced in a solid target by high intensity, femtosecond laser pulses. Our pump-probe measurements and PIC simulations clearly establish the power-law behavior of the magnetic field. We believe that our results will have important implications for understanding phenomena affected by plasma turbulence, for example turbulent induced resistivity and how it may affect the fast ignition of laser fusion by such hot electron jets. They also open the possibility for laboratory simulations of turbulent structures in stellar environments.

Methods

Experimental. The experiments were performed using a 20 terawatt Ti:sapphire chirped pulse amplification laser at the Tata Institute of Fundamental Research, Mumbai, delivering 30 fs, 800 nm pulses at repetition rate of 10 Hz. The schematic of the experimental setup is shown in Fig. 1. The *p*-polarized laser pump pulse was incident at an angle 40° with respect to the target normal and focused to 17 μm spot with a $f/3$ off-axis parabola on an optically polished aluminum coated BK-7 glass target. The thickness of the aluminum coating on the BK-7 glass is kept much larger than the skin depth ($\delta_s \sim c/\omega_p \sim 100$ nm). So the incident pump laser interacts only with the aluminum coating and creates plasma on aluminum layer and hot electron can propagates through the glass of lower conductivity. The pulse energy on target is 120 mJ, giving a peak intensity of $\sim 3\times10^{18}\,\mathrm{W/cm^2}$. The normalized classical momentum of the electron in the laser electric field is given by $a = P_{\mathrm{osc}}/mc = eE/(m\omega_0 c) = 8.53\times10^{-10}\times(I\lambda^2)^{1/2}$, where *e* is the electron charge, *E* is the electric field at focus, *m* is electron's mass, ω_0 is the laser angular frequency, *c* is the speed of light, *I* is the intensity of light in W/cm^2 and λ is the laser wavelength in microns. Relativistic intensities are reached when *a* is about or greater than unity; in the present case, $a = 1.2$.

The target was placed inside a vacuum chamber at a pressure of 10^{-5} Torr and was rastered using computer controlled $xyz\theta$ precision motion stage assembly to ensure that each laser pulse irradiates a fresh spot on the target. We extracted 5% of the main beam and converted that to the second harmonic (2ω) (400 nm) and used as a probe, so that it can penetrate up to four times the critical density that corresponds to 800 nm (36). Another advantage of using 2ω probe is the suppression of pump noise (36). The probe was time delayed by a high precision translation stage. The intensity of probe was kept very low, approximately $10^{11}\,\mathrm{W/cm^2}$, by focusing it loosely on the target (spot size of approximately 60 μm). The spatial overlap of pump and probe pulses was achieved by viewing the interaction region with a video zoom microscope coupled to a CCD camera. The temporal matching (i.e., time delay = 0 ps) of the pump and the probe pulses was ascertained by the sharp transition in the temporally resolved reflectivity of the probe pulse, indicating formation of the plasma by the pump pulse (15, 16). The incident polarization of the probe pulse was adjusted using a half-wave plate and its reflected polarization state was measured by a Glan-air analyzer with an extinction ratio of $1:10^{-5}$.

The transverse spatial profile of the intensity of the reflected probe pulse at the parallel ($I_{\parallel}$) and the crossed ($I_{\perp}$) positions of the analyzer was measured by a CCD camera with a pixel size of 6.45×6.45 μm and an imaging array of $1{,}392\times1{,}040$ pixels. The probe pulse is influenced by the fast electron generated magnetic field in the plasma, undergoing a change in its polarization ellipse, via the magneto-optic Cotton–Mouton effect (15–17, 19). Typically, the four Stokes' Parameters are measured for inferring the complete polarization state of the reflected probe. Of particular relevance are the parallel and crossed components of polarization. For this, the reflected probe is divided into two arms so that both can be measured simultaneously. In each arm there are two detectors—a photomultiplier tube to measure space integrated ellipticity and a CCD camera to measure spatially resolved ellipticity. Magnetic field can be derived from the induced ellipticity by using equation $\beta(t) = (e^2/m_e c^3 \omega n_c)\int n_e(l,t)B^2(l,t)dl$ (19). In brief, it can be shown that the Stokes' vector in the magnetized plasma evolves in the direction of the propagation of the laser pulse, depending on the self-generated magnetic field. The plasma box is divided into a large number of slabs, where the plasma parameters are assumed to be approximately constant in a given slab. The output Stokes' vector of one slab is fed into the next slab as the input and the evolution equation of the Stokes' vector is solved numerically in each slab to finally yield the ellipticity (and hence the magnetic field) of the laser pulse emerging from the plasma box. An exponential plasma density profile was used for the numerical integration with a plasma expansion velocity of 5×10^6 cm/sec derived from Doppler shift measurement of the reflected probe from plasma (36). The above procedure was implemented for each CCD pixel to get a 2D spatial mapping of the magnetic field at the critical surface of the 400-nm probe beam.

Turbulence Analysis. The power spectra have been calculated as follows. The transverse profile of magnetic field image $[B(x,y)]$ is converted into spatial Fourier transform $[B(k_x,k_y)]$ image. Two-dimensional power spectrum $[P(k_x,k_y)]$ is calculated from $[B(k_x,k_y)]$ by using

$$P(k_x,k_y) = B(k_x,k_y) * \mathrm{conj}[B(k_x,k_y)]. \qquad \textbf{[1]}$$

The 1D power spectrum $[Q(k_x)$ and $Q(k_y)]$ is obtained as follows:

$$Q(k_x) = \int P(k_x,k_y)dk_y \qquad \textbf{[2]}$$

$$Q(k_y) = \int P(k_x,k_y)dk_x. \qquad \textbf{[3]}$$

PIC Simulations. We have conducted a series of 2D-PIC simulations with a code developed following the scheme described in refs. 37–39. In our code, binary collisions between electrons and electrons-ions are included as per the scheme in refs. 40 and 41. Absorption and periodic boundary conditions are adopted in the *z* direction and *y* direction, respectively. Particles leaving from the simulation box are reflected with random initial thermal velocities. The simulation box is $16\lambda\times96\lambda$ with 32 cells in a laser wavelength λ. There are 25 particles per cell per species. In our simulations, aluminum targets are used. Plasma density is uniform along the *y* direction and exponentially grows along the *z* direction as $n_c\exp(z/L-1)$ to a plateau at $140n_c$, where $L = 2\lambda$ is the scale length. The initial temperature of the electrons and ions are 10 eV and 1 eV, respectively (note that the simulation results do not depend upon the initial electron temperature, in particular at the later stages of evolution). *P*-polarized laser is incident at 45° angle on the target with an intensity of $3.0\times10^{18}\,\mathrm{W/cm^2}$, the wavelength ($\lambda$) of 800 nm. The laser field profile is $a = a_0\sin^2(\pi t/\tau)\exp(y^2/\omega_0^2)$, the laser pulse duration (τ) is 20 laser cycles (53 fs), and the waist (w_0) is 10λ.

ACKNOWLEDGMENTS. A.D. acknowledges discussions with E. Bodenschatz, G. Falkovich, and S. Malensowski at the KITP workshop on Nature of Turbulence in 2011. G.R.K. and A.D. acknowledge their respective DAE-SRC-ORI grants (Government of India). G.R.K. also acknowledges a J.C. Bose Fellowship from the Department of Science and Technology (Government of India). Z.M.S. acknowledges the support from the Natural Science Foundation of China (Grants 11075105 and 11121504).

1. Tatarakis M, et al. (2002) Laser technology: Measuring huge magnetic fields. *Nature* 415:280.
2. Wagner U, et al. (2002) Laboratory measurements of 0.7 GG magnetic fields generated during high-intensity laser interactions with dense plasmas. *Phys Rev E Stat Nonlin Soft Matter Phys* 70:026401.
3. Belyaev VS, Krainov VP, Lisitsa VS, Matafomov AP (2008) Generation of fast charged particles and superstrong magnetic fields in the interaction of ultrashort high-intensity laser pulses with solid targets. *Physics-Uspekhi* 51:793–814.
4. Tabak M, et al. (1994) Ignition and high gain with ultrapowerful lasers. *Phys Plasmas* 1:1626–1634.
5. Kodama R, et al. (2001) Fast heating of ultrahigh-density plasma as a step towards laser fusion ignition. *Nature* 412:798–802.
6. Jeanloz R, et al. (2007) Achieving high-density states through shock-wave loading of precompressed samples. *Proc Natl Acad Sci USA* 104:9172–9177.
7. Murane MM, Kapteyn HC, Rosen MD, Falcone RW (1991) Ultrafast X-ray pulses from laser-produced plasmas. *Science* 251:531–536.

8. Falgarone E, Passot T (2003) *Turbulence and Magnetic Fields in Astrophysics, Lecture Notes in Physics* (Springer, Berlin, Heidelberg).
9. Nordhaus J, Wellons S, Spiegel DS, Metzger BD, Blackman EG (2011) Formation of high-field magnetic white dwarfs from common envelopes. *Proc Natl Acad Sci USA* 108:3135–3140.
10. Drake RP (2006) *High-Energy-Density Physics-Fundamentals, Inertial Fusion and Experimental Astrophysics* (Springer, Berlin, Heidelberg).
11. Sentoku Y, Mima K, Kaw P, Nishikawa K (2003) Anomalous resistivity resulting from MeV-electron transport in overdense plasma. *Phys Rev Lett* 90:155001.
12. Yabuuchi T, et al. (2009) Evidence of anomalous resistivity for hot electron propagation through a dense fusion core in fast ignition experiments. *New J Phys* 11:093031.
13. Weibel ES (1959) Spontaneously growing transverse waves in a plasma due to an anisotropic velocity distribution. *Phys Rev Lett* 2:83–84.
14. Pukhov A (2003) Strong field interaction of laser radiation. *Rep Prog Phys* 66:47–101.
15. Sandhu AS, et al. (2003) Laser-generated ultrashort multimegagauss magnetic pulses in plasmas. *Phys Rev Lett* 89:225002.
16. Sandhu AS, Kumar GR, Sengupta S, Das A, Kaw PK (2006) Real-time study of fast-electron transport inside dense hot plasmas. *Phys Rev E Stat Nonlin Soft Matter Phys* 73:036409.
17. Kahaly S, et al. (2009) Polarimetric detection of laser induced ultrashort magnetic pulses in overdense plasma. *Phys Plasmas* 16:043114.
18. Krommes JA (2002) Fundamental statistical descriptions of plasma turbulence in magnetic fields. *Phys Rep* 302:1–65.
19. Segre SE (1999) A review of plasma polarimetry—theory and methods. *Plasma Phys Controlled Fusion* 41:R57–R100.
20. Batchelor GK (1987) *An introduction to fluid dynamics* (Cambridge Univ Press, Cambridge, UK).
21. Warhaft Z (2002) Turbulence in nature and in the laboratory. *Proc Natl Acad Sci USA* 99:2481–2486.
22. Mulser P, Bauer D (2010) *High power laser-matter interaction, Ch. 5* (Springer, Berlin, Heidelberg), Springer Tracts in Modern Physics 238.
23. Cox JL, Thomas LH (1970) Current induced in a plasma by a penetrating electron beam. *Proc Natl Acad Sci USA* 67:1651–1655.
24. Pukhov A (2001) Three-dimensional simulations of ion acceleration from a foil irradiated by a short-pulse laser. *Phys Rev Lett* 86:3562–3565.
25. Honda M, Meyer-ter-Vehn J, Pukhov A (2000) Two-dimensional particle-in-cell simulation for magnetized transport of ultra-high relativistic currents in plasma. *Phys Plasmas* 7:1302–1308.
26. Sentoku Y, et al. (2002) Three-dimensional particle-in-cell simulations of energetic electron generation and transport with relativistic laser pulses in overdense plasmas. *Phys Rev E Stat Nonlin Soft Matter Phys* 65:046408.
27. Yadav SK, Das A (2010) Nonlinear studies of fast electron current pulse propagation in a two dimensional inhomogeneous plasma. *Phys Plasmas* 17:052306.
28. Jain N, et al. (2007) Role of current shear driven turbulence in anomalous stopping of energetic electrons. *Phys Lett A* 363:125–129.
29. Das A, Kaw PK (2001) Nonlocal sausage-like instability of current channels in electron magnetohydrodynamics. *Phys Plasmas* 8:4518–4523.
30. Wei MS, et al. (2004) Observations of the filamentation of high-intensity laser-produced electron beams. *Phys Rev E Stat Nonlin Soft Matter Phys* 70:056412.
31. Fuchs J (2003) Spatial uniformity of laser-accelerated ultrahigh-current MeV electron propagation in metals and insulators. *Phys Rev Lett* 91:255002.
32. Jung R (2005) Study of electron-beam propagation through preionized dense foam plasmas. *Phys Rev Lett* 94:195001.
33. Kingsep AS, Chukbar KV, Yankov VV (1990) Electron magnetohydrodynamics. *Rev Plasma Phys* 16:243–288.
34. Hao B, Sheng ZM, Ren C, Zhang J (2009) Relativistic collisional current-filamentation instability and two-stream instability in dense plasma. *Phys Rev E Stat Nonlin Soft Matter Phys* 79:046409.
35. Biskamp D, Schwarz E, Drake JF (1996) Two-dimensional electron magnetohydrodynamic turbulence. *Phys Rev Lett* 76:1264–1267.
36. Mondal S, et al. (2010) Doppler spectroscopy for ultrafast temporal mapping of density dynamics in laser-induced plasmas. *Phys Rev Lett* 105:105002.
37. Birdsall CK, Langdon AB (1985) *Plasma Physics via Computer Simulation* (McGraw-Hill, New York).
38. Esirkepov TZ (2001) Exact charge conservation scheme for Particle-in-Cell simulation with an arbitrary form-factor. *Comput Phys Commun* 135:144–153.
39. Villasenor J, Buneman O (1992) Rigorous charge conservation for local electromagnetic field solvers. *Comput Phys Commun* 69:306–316.
40. Cadjan MG, Ivanov MF (1999) Langevin approach to plasma kinetics with Coulomb collisions. *J Plasma Phys* 61:89–106.
41. Sentoku Y, et al. (1998) Effects of relativistic binary collisions on PIC simulation of laser plasmas. *J Phys Soc Japan* 67:4084–4088.